Steel and Composite Structures, *Vol. 15, No. 6 (2013) 679-703*
DOI: http://dx.doi.org/10.12989/scs.2013.15.6.679

Fundamental behavior of CFT beam-columns under fire loading

Amit H. Varma [*1], Sangdo Hong [2a] and Lisa Choe [3b]

[1] *School of Civil Engineering, Purdue University, 550 Stadium Mall Drive West Lafayette, Indiana 47907, USA*
[2] *Indiana Department of Transportation, West Lafayette, Indiana, USA*
[3] *National Institute of Standards and Technology, Gaithersburg, Maryland, USA*

(*Received February 02, 2012, Revised August 26, 2013, Accepted September 09, 2013*)

Abstract. This paper presents experimental investigations of the fundamental behavior of concrete filled steel tube (CFT) beam-columns under fire loading. A total of thirteen specimens were tested to determine the axial force-moment-curvature-temperature behavior of CFT beam-columns. The experimental approach involved the use of: (a) innovative heating and control equipment to apply thermal loading and (b) digital image correlation with close-range photogrammetry to measure the deformations (e.g., curvature) of the heated region. Each specimen was sequentially subjected to: (i) constant axial loading; (ii) thermal loading in the expected plastic hinge region following the ASTM E119 temperature-time *T-t* curve; and (iii) monotonically increasing flexural loading. The effects of various parameters on the strength and stiffness of CFT beam-columns were evaluated. The parameters considered were the steel tube width, width-to-thickness ratio, concrete strength, maximum surface temperature of the steel tube, and the axial load level on the composite CFT section. The experimental results provide knowledge of the fundamental behavior of composite CFT beam-columns, and can be used to calibrate analytical models or macro finite element models developed for predicting behavior of CFT members and frames under fire loading.

Keywords: fire; columns; composite; experiments; temperature

1. Introduction

Steel-concrete composite structures are considered for many construction projects because of their structural efficiency, cost benefits and construction economy. Composite construction is also attractive from a fire resistance perspective. Steel structures utilizing composite columns can potentially achieve high fire resistance due to the presence of concrete, which has good fire resistance characteristics. Concrete filled steel tube (CFT) columns are an excellent example of composite construction and its efficiencies and advantages.

Some of the major advantages of composite construction using CFT columns are as follows: (i) the steel framework can be erected independently during concrete placement; (ii) The steel tube acts as formwork for casting concrete thus improving the construction schedule and economy; (iii) The concrete infill restrains the inward buckling of the steel tube (Patel *et al*. 2012); (iv) The steel

∗Corresponding author, Associate Professor, E-mail: ahvarma@purdue.edu
[a] Ph.D., E-mail: shong@indot.in.gov
[b] Ph.D., E-mail: lisa.choe@nist.gov

http://www.techno-press.org/?journal=scs&subpage=8 ISSN: 1229-9367 (Print), 1598-6233 (Online)

tube provides some nominal confinement to the concrete infill; and, (v) under fire loading, the concrete infill acts as a heat sink to delay the heating of the steel tube and maintains its strength for longer durations of heating (Hong and Varma 2010).

The current building codes emphasize prescriptive fire resistant design, while providing some options and guidance for performance-based fire resistant design. The building codes prescribe required fire resistance rating (required FRR) for the primary structural components of the building. These FRR requirements are: (i) based on the building geometry, use, and occupancy details; and (ii) specified in terms of the hours of standard ISO-834 (1980) or ASTM E119 (2010) fire time-temperature (*T-t*) curve they can withstand. Fire resistant design is achieved by selecting structural components and fire protections with design fire resistance rating (design FRR) values greater than or equal to the required FRR.

The design FRR values for structural components can be obtained from: (1) standard fire tests conducted according to ISO-834 (1980) or ASTM E119 (2010); or (2) standard calculation methods based on the experimental results and regression analyses of earlier standard fire test results (e.g., ASTM E119 (2010), NFPA (2009), ASCE/SEI/SFPE (2007)). Thus, the standard fire test forms the basis of the prescriptive fire resistant design approach, and most prior work in the U.S. has focused on evaluating the design FRR values of structural components.

2. Motivation and research need

Standard fire tests have been conducted by several researchers (e.g., Xu *et al*. (2011), Lu *et al*. (2010a, 2010b), Huo *et al*. (2011), Romero *et al*. (2011), Kodur and Mackinnon (2000), Sakumoto *et al*. (1994), Han *et al*. (1994)) to determine the design FRR values for composite CFT columns. These tests were conducted using gas furnaces that were specially designed and commissioned to test column specimens by subjecting them to combined axial loads and heating (e.g., Sakumoto *et al*. (1994), Romero *et al*. (2011), Lu *et al*. (2010a, b), Huo *et al*. (2011)). The axial loads were applied and maintained constant during the test, and the heating was controlled to subject the air surrounding the column specimens to the standard (ISO-834 (1980), ASTM E119 (2010)) gas phase (air) temperature-time (*T-t*) curve. These column furnaces are usually quite expensive to build, maintain and use.

The elevated temperatures and heat flux within the furnaces prevent the use of conventional voltage based sensors (strain gages, displacement transducers, etc.) for measuring the structural behavior (strains, deflections, rotations, etc.) of the column specimens. Hence, the results from the standard fire tests are limited to: (1) the thermal *T-t* responses of the column surfaces and several points within the cross-section; (2) the overall axial displacement-time responses, and in some cases (e.g., Sakumoto *et al*. (1994), Romero *et al*. (2011), Lu *et al*. (2010b)); (3) the midspan lateral displacement-time responses of the column specimens. These results can be used to calculate the time to failure and the design FRR values for the column specimens.

The results from standard fire tests do not provide knowledge or insight into the fundamental force-deformation behavior of columns under fire loading. They cannot be used directly or indirectly to estimate the behavior of columns or other members for any other structural or thermal loading and boundary conditions. These limitations of the standard fire test and the prescriptive fire resistant design approach are well known and documented in several sources (e.g., AISC Design Guide 19 (2003), Beyler *et al*. (2007)).

As discussed in Maluk *et al*. (2012a), Maluk and Bisby (2012b), there is a significant need for innovative experimental methods and analytical approaches that can be used to: (1) investigate the fundamental behavior of structural members and systems under realistic fire loading; (2) evaluate the effects of various structural and fire loading parameters on behavior and collapse; and (3) develop rational structural behavior-based fire resistant design provisions. This need is further endorsed by the findings and the future research recommendations from the 9/11 World Trade Center (WTC) Towers collapse investigations conducted by the National Institute for Standards and Technology, Building and Fire Research Laboratory (NIST BFRL) researchers (e.g., Sunder *et al*. (2005), NIST NCSTAR 1A (2008)). Similar research needs have been identified by recent national workshops and publications focusing on structural fire engineering research needs (e.g., Beyler *et al*. (2007), Kodur *et al*. (2008)). The structural engineering research and practice communities will have to work collaboratively to make progress and address these research needs in the near future.

3. Research objectives and significance

The authors have contributed to this progress by conducting a research project focusing on the fundamental behavior and stability of composite CFT columns under standard fire loading (Hong 2007). This project included three major tasks: (1) Development and verification of numerical (3D finite element) models for simulating the fire behavior of CFT columns. (2) Experimental investigations of the fundamental force-deformation-temperature (F-δ-T) behavior of CFT members subjected to fire loading. And, (3) using the fundamental F-δ-T behavior to develop and verify analytical approaches for predicting the behavior and stability failure of CFT columns under fire loading.

The results from all three tasks have been presented in detail in Hong (2007). Additionally, the results from Tasks 1 and 3 have been summarized in Hong and Varma (2009, 2010), respectively. This paper presents the results from Task 2 in detail. The paper presents:

(1) An innovative experimental approach that was developed to determine the fundamental behavior, namely, the section moment-curvature (M-ϕ) behavior of structural members subjected to elevated temperatures from fire loading.
(2) The results of experimental investigations conducted on CFT beam-column members to determine their section M-ϕ responses at elevated temperatures, and the effects of parameters, namely, axial loading, heating, concrete strength, tube geometry, and fire protection thickness on them.
(3) The development of simple equations that can be used to estimate the stiffness and strength of CFT beam-columns members at elevated temperatures from fire loading.

3.1 Research significance

The experimental approaches described in this paper present the flexibility of the method originally developed by Hong (2007). The beam-column tests described in this paper can be conducted in traditional structural engineering laboratories using conventional hydraulic equipment and actuators to apply mechanical loading and the radiation-based heating equipment for applying simultaneous heating (thermal loading). Since the specimens are not placed inside furnaces, their behavior can be observed visually and their thermally induced responses (displacements, strains, and curvatures, etc.) can be measured extensively using close-range photogrammetry (Sadek *et al*. 2003).

The experimental results presented in this paper provide insight into the fundamental behavior of CFT members, and can be used to estimate the stiffness and strength of CFT members under fire loading. The experimental results can be used to benchmark new or existing analytical models developed to model or predict the behavior of CFT members in building structures subjected to fire loading. The authors (Hong and Varma 2010) used the experimental results to develop and benchmark an analytical approach for predicting the stability failure of CFT columns under fire loading.

In addition, Choe *et al*. (2011) recently investigated the fundamental behavior of wide-flange steel members by implementing the experimental approach presented in this paper. Full-scale steel columns and beam-columns, typically used in steel building structures, were tested under combined thermal and mechanical loads to investigate the fundamental P-M-ϕ-T behavior of failure sections subjected to elevated temperatures simulating fire. Simple analytical models were also developed to estimate the fundamental force-displacement and moment-curvature behavior of steel members using Newmark's approach as presented in Hong and Varma (2010). The analytical models of wide-flange steel columns under fire loading were verified by Choe (2011). Also, the column test data have been used for developing and validating existing column design curves that account for the effects of surface temperatures (e.g., Choe 2011, Agarwal and Varma 2011). The fundamental test data obtained from the experimental approach presented in this paper can eventually be used to develop a closed-form analytical model to present the moment-curvature behavior of load-bearing members subjected to combined mechanical and thermal loading (Walz *et al*. 2011).

4. Experimental approach

The experimental approach was developed to determine the fundamental thermal and structural behavior of structural members under fire loading. Two types of tests were conducted: (1) to measure the heat transfer behavior and thermal T-t (temperature-time) response of various points in the member cross-section, and (2) to measure the moment-curvature M-ϕ behavior of the member section subjected to elevated temperatures from fire loading.

4.1 Heat transfer experiments and heating equipment

The focus of the heat transfer experiments was on the applied thermal loading, and the measured temperature-time (T-t) responses of points in the member cross-section. The structural loads were not applied in this experiment to focus on the thermal response of the member cross-section. The thermal loading was applied to the member cross-section using ceramic fiber radiant heaters. These heaters use radiation based heating to apply the thermal loads, and are capable of providing operating temperatures up to 1200°C (2200°F) with applied heat flux densities of 0.8 to 4.6 W/cm^2. These heating units are made by integrating iron-chrome-aluminum heating elements within lightweight alumina-silica fiber composite panels. The ceramic fiber heaters used in this test had dimensions of 355×305 mm, heating area of 305×305 mm, and heat flux or watt density of 3.2 W/cm^2. Four ceramic fiber heaters were placed around the sides of the member to enclose the section the section and thus apply thermal loading.

Standard fire tests (e.g., ASTM E119 (2010)) are typically conducted in special gas furnaces, where the standard provides the target T-t curve for heating the air surrounding a structural member. However, this gas phase (air) *T-t* curve cannot be used as the target *T-t* curve to control the ceramic fiber heaters because they use radiation to directly heat the exposed surfaces of the structural members. Therefore, the *T-t* responses of the exposed surfaces of structural members subjected to standard (E119) heating were computed analytically, and used as the target *T-t* curves to control the radiant heating equipment. The *T-t* responses of the exposed surfaces were computed using a finite difference method analysis of the heat balance equations and were verified using experimental measurements by the authors (Hong and Varma 2009, 2010). The heat transfer analysis was conducted using in-house software, which implemented the finite different method to solve the heat balance equations numerically. Details of the numerical approach are presented in Hong and Varma (2010) and not repeated here for brevity. The computed surface *T-t* curves were used as the target *T-t* curves for controlling the radiant heating equipment.

The temperature control network for each heater consists of four elements, namely, a temperature controller, a power controller, a heating unit, and a temperature sensor. The temperature sensor was a K-type thermocouple that was attached to the exterior surface of the member being heated. The other end of the thermocouple was connected to the analog input terminal on the temperature controller. The power controller was connected to the output terminal of the temperature controller, and the heating unit (ceramic fiber radiant heater) was connected to the power controller. The target *T-t* curve for the exposed surface was divided into sixteen small steps and input to the temperature controller using ramp time functions. The temperature controller monitors the thermocouple and determines whether the power controller needs to be switched on or off to achieve the target *T-t* curve on the exposed surface. The power controller is attached to the heating units, which switch the heating on or off depending on the power controller. Several thermocouples were used to measure the surface *T-t* responses, and those for various points in the member cross-sections.

4.2 Beam-column experiments

The focus was on conducting short beam-column tests to determine the fundamental moment-curvature (M-ϕ) response of the anticipated plastic hinge region subjected to combined axial load, flexural loading, and elevated temperatures from fire loading. The beam-column specimens were fixed at the base and free at the top. The heating was applied to the base of the beam-column specimen in the anticipated plastic hinge region.

The heating was applied using the same ceramic fiber radiant heaters and temperature control network as the heat transfer experiments. It was controlled to simulate the effects of standard (E119) fire loading on the exposed surfaces as described earlier. After a specific time of heating (e.g., 1-2 hours), lateral loading was applied monotonically to the top of the specimen. The moment-curvature (M-ϕ) behavior of the plastic hinge at the base of the beam-column subjected to constant axial load, heating, and monotonically increasing flexural loading was measured using digital cameras and close-range photogrammetry described in Hong (2007) and Choe *et al*. (2011), and summarized briefly here.

4.3 Measuring deformations at elevated temperatures

Traditional voltage based sensors could not be used to measure the deformations of the heated plastic hinge region due to the elevated temperatures. Two-dimensional digital imaging was used instead to measure the longitudinal and transverse displacements of target points (or regions) located in the plastic hinge region of the beam-column base. These measurements were then used to compute the deformations and curvature of the heated plastic hinge region.

A set of high quality grayscale digital cameras that were specially designed for close-range photogrammetry applications were used to capture digital images of each of the target regions. The focal length of the digital cameras was set at 450 mm, and they were installed perpendicular to the target regions such that the effects of lens distortion were negligible. After installation, a specially designed pre-dimensioned grid image was used to calibrate the pixel size in the target region as described in Hong (2007). A reference image consisting of four small white circles (dots) on black steel background was made in each of the target regions.

The Labview-vision module was used to control and acquire image data from the digital cameras. Prior to starting the test, the target region images were acquired and the reference images were identified. During the test, the Labview vision module was used to trigger the cameras at every second, and the acquired images were stored in the data acquisition computer via a frame grabber board. After completing the test, the digital image correlation (DIC) program in the Labview-vision module was used to locate and track the pre-selected reference image in the acquired target region images using pattern matching (Selden 2010). The displacement of the reference image in these sequentially acquired images was calculated using pattern matching and the pixel size calibration done earlier. Thus, the DIC post-processing results included the horizontal (X) and vertical (Y) displacements of the reference images in each of the corresponding target regions. Additional details and the calibration and verification of this process for measuring deformations at elevated temperatures are presented in Hong (2007) and Selden (2010).

5. CFT Heat transfer test results

5.1 Test Setup, Matrix, and Instrumentation Layout

Fig. 1(a) shows a picture of the test-setup for conducting the heat transfer tests on CFT members. As shown, ceramic fiber heaters were placed on each of the four sides of the CFT member. The heaters were individually controlled to subject the sides of the CFT members to thermal loading. The target T-t curves for the exposed surfaces of the members were based on those calculated using the finite difference method shown in Hong and Varma (2009).

Table 1 summarizes the test matrix for the heat transfer tests. The specimen nomenclature consists of the tube size in inches, tube width-to-thickness (b/t) ratio, concrete strength (f'_c) in ksi, and fireproofing thickness in inches. All the specimens were made from 305 × 305 × 9.5 mm (12 × 12 × 3/8 in.) steel tubes made from ASTM A500 Grade-B steel. The details of the concrete mix proportion are reported in Hong (2007). The concrete mix was made using crushed limestone (carbonate) aggregate. Table 1 includes the measured moisture content of the concrete on the day of test. The relative humidity was not measured. Specimens 1 and 2 were filled with 4 ksi (27 MPa) nominal compressive strength concrete, and Specimens 3 and 4 were filled with 9 ksi (62 MPa) nominal compressive strength concrete. The corresponding measured compressive strengths on the day of the tests are shown in Table 1.

Gypsum plaster (Gold Bond Gypsolite plaster) was used as the fire proofing material for this research. Metal lath was first placed around the steel tube of the CFT members. After the metal lath was secured, gypsum plaster was mixed according to the manufacturer recommendations, and placed on the metal lath using hand-finishing trowels. The gypsum plaster thickness was monitored carefully during application. As shown in Table 1, two different gypsum plaster thickness were considered. Specimens 1 and 4 had plaster thickness of 13 mm (1/2 in.), and Specimens 2 and 3 had plaster thickness of 6.4 mm (1/4 in.).

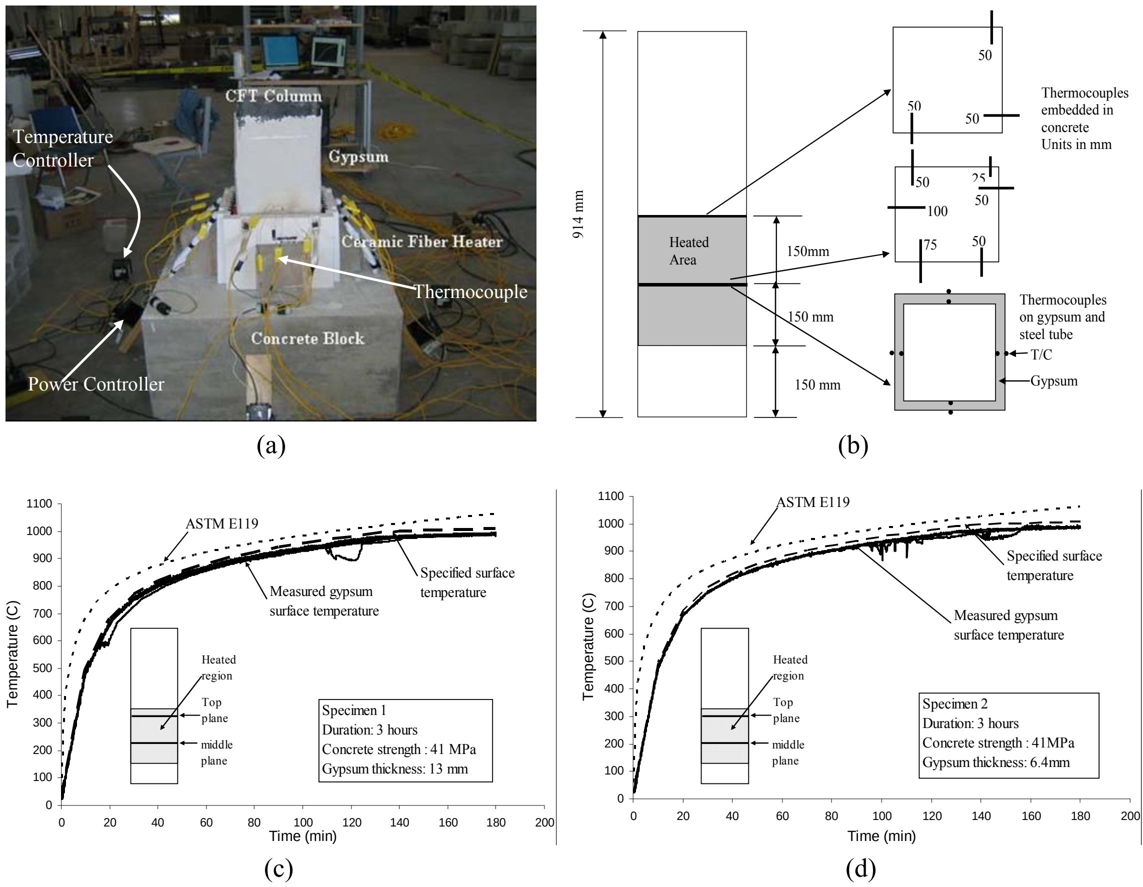

Fig. 1 Heat transfer test setup and results: (a) photograph; (b) instrumentation; (c) specified and measured *T-t* curves for Specimen 1; and (d) Specimen 2

Table 1 Test matrix for CFT heat transfer specimens

Specimen No.	Specimen ID	Tube Size (mm × mm)	Concrete f'_c (MPa) (nominal)	Concrete f'_c (MPa) (measured on day of test)	Gypsum thickness (mm)	Moisture content (%)
1	CFT-12-34-4-1/2	305 × 9.5	27	41.4	13	7
2	CFT-12-34-4-1/4	305 × 9.5	27	41.4	6.4	7
3	CFT-12-34-9-1/4	305 × 9.5	62	68.9	6.4	4
4	CFT-12-34-9-1/2	305 × 9.5	62	68.9	13	4

All the heat transfer tests were conducted on CFT columns with gypsum plaster because the fire protection of exposed steel is recommended in the U.S. Earlier studies (Varma, Srisa-ard, and Hong 2004) had also indicated that the bare steel tube heats up very rapidly, while the concrete infill remains relatively cold. This reduces the flexural capacity very quickly because it depends on the tension contribution of the heated steel tube. The flexural capacities of bare steel and fire protected steel CFT columns are comparable depending on the temperature of the steel tube; however, the heating time for bare steel CFT columns can be very short. Fire protection of CFT beam-columns is recommended because of this reason.

Fig. 1(b) shows the instrumentation layout for the heat transfer tests. As shown, on each side of the CFT member, thermocouples were attached to the exterior surfaces of the gypsum plaster and the steel tube under the gypsum plaster. These thermocouples were centered about the heating area. Additionally, thermocouples were embedded in the concrete infill to measure temperatures at 25, 50, 75, and 100 mm depth. The concrete infill temperatures were measured at the middle and top planes of the heating area.

Thermocouple installation is explained in detail in Hong (2007). Small (6 mm) diameter holes were drilled on all four sides of the steel tube for thermocouple installation prior to concrete placement. Heat-shrink tubes were placed on the bare thermocouple wires in order to provide protective insulation for electrical interference from the steel tube and water in the concrete. Concrete was slowly placed to minimize shifting of thermocouples inside the steel tubes. Although extra care was taken, some of embedded thermocouples may have shifted slightly during concrete casting.

5.2 Test results and comparisons

Figs. 1(c)-(d) show comparisons of the specified target *T-t* curves and the measured *T-t* curves on the exposed surfaces of Specimens 1 and 2 with gypsum plaster thicknesses of 13 and 6.4 mm, respectively. These comparisons are typical and similar to those obtained for all other tests. They show that the specified and measured *T-t* curves are almost identical, which demonstrates the efficiency of the heating units and temperature control.

Fig. 2(a) shows the *T-t* curves measured on the surfaces of the steel tube of Specimen 1 (with 13 mm gypsum plaster). The measured steel temperatures were about 390°C at the middle plane after three hours of heating and about 260°C at the top plane. The variations in the measured steel surface *T-t* responses are very small. The heat loss at the top planes is due to the limitation of heating arrangement and the type of heaters used in the test. Although flat heaters were used, they were not in contact with the specimen surfaces to prevent electrical (safety) hazards associated with metal thermocouples contacting the hot electrical elements. The small gap between the heaters and the specimen caused some heat loss from the top.

Fig. 2(b) shows the measured *T-t* curves for the concrete infill at various depths (25, 75, and 100 mm). The concrete temperatures at the middle plane were higher than the temperatures at the top plane, because some of the heat is lost to the unheated sections above. Additional temperature measurements and *T-t* responses are provided in Hong (2007). The measured *T-t* responses for Specimen 4, which had the same gypsum plaster thickness (13 mm) but slightly higher concrete strength ($f'_c = 68.9$ MPa), were similar to those shown in Figs. 2(a)-(b). The results for Specimen 3 are included in Hong (2007), and not presented here for brevity.

Fig. 2(c) shows the *T-t* curves measured on the steel tube surfaces of Specimen 3 (with 6.4 mm thickness gypsum plaster). The measured steel temperatures were about 580°C at the middle plane after three hours of heating and about 420°C at the top plane. The variations in the measured steel surface *T-t* responses are very small. Fig. 2(d) shows the measured *T-t* curves for the concrete infill at various depths (25, 75, and 100 mm). The concrete temperatures at the middle plane were higher than the temperatures at the top plane, because some of the heat is lost the unheated sections above. Additional temperature measurements and *T-t* responses of the steel tubes and their comparisons are provided in Hong (2007). The measured *T-t* responses for Specimen 2, which had the same gypsum plaster thickness (6.4 mm) but slightly lower concrete strength ($f'_c = 41.4$ MPa), were similar to those shown in Figs. 2(c)-(d). The results for Specimen 2 are included in Hong (2007), and not presented here for brevity.

The heat transfer test results (*T-t* curves) were compared with each other to evaluate the effects of concrete strength and fireproofing thickness on the thermal response of CFT specimens. These comparisons are detailed in Hong (2007) and summarized briefly here. The steel tube surface and the concrete infill *T-t* curves for Specimens 1 and 2 (with 13 mm gypsum plaster but different concrete strengths) were quite similar to each other. Similarly, the steel tube surface and concrete infill *T-t* curves for Specimens 3 and 4 (with 6.4 mm gypsum plaster but different concrete

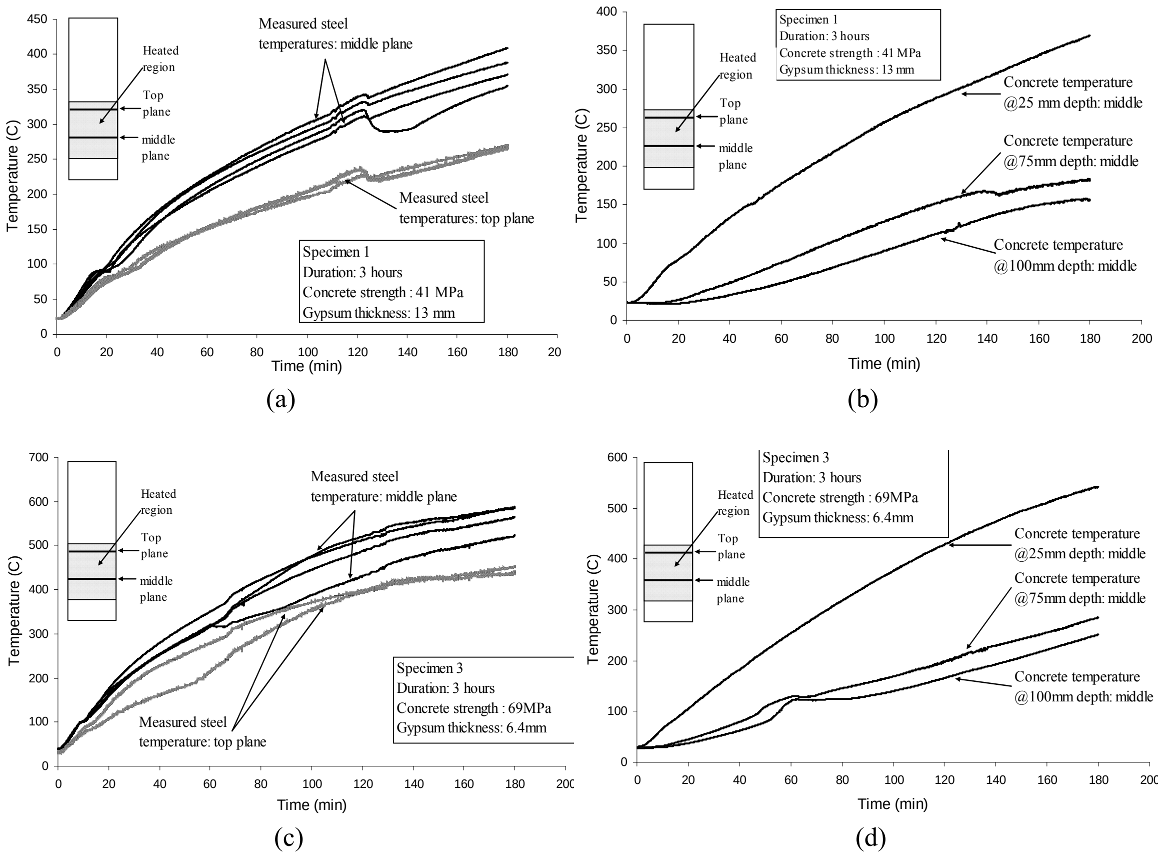

Fig. 2 Heat transfer test results: (a) steel *T-t* curves for Specimen 1; (b) concrete *T-t* curves for Specimen 1; (c) steel *T-t* curves for Specimen 3; (d) concrete *T-t* curves for Specimen 3

strengths) were also quite similar to each other. Different concrete strengths (f'_c = 41.4 or 68.9 MPa) do not seem to have a significant influence on the thermal response of the CFT specimens. It is important to note that both of these were normal-weight concrete mixes with very similar aggregates.

The steel tube surface and the concrete infill *T-t* curves for Specimens 1 and 2 (with same concrete strength f'_c = 41.4 MPa but different gypsum plaster thickness) were quite different. Similarly, the steel tube surface and the concrete infill *T-t* curves for Specimens 3 and 4 (with same concrete strength f'_c = 68.9 MPa but different gypsum plaster thickness) were also quite different. As expected thinner fireproofing material yields higher temperatures on the steel surfaces and inside the concrete infill, while thicker fireproofing yields lower temperatures on the steel surfaces and inside the concrete infill.

6. CFT beam-column tests

6.1 Test setup, matrix, and materials

Fig. 3 shows a photograph of the test setup used for subjecting CFT beam-column specimens to combined axial, flexural, and thermal loading as follows. The total length of the CFT specimens was 2.45 m. The bottom 0.6 m of the specimen length was post-tensioned to two concrete blocks, which were then post-tensioned to the laboratory strong floor. This provided a fixed boundary condition at the base of the CFT specimens.

The CFT specimens were subjected to axial loading at the top using a specially designed axial loading arrangement consisting of a 4500 kN capacity hydraulic ram, loading beam, two threaded rods and pin and clevis arrangement. As shown in Fig. 3, the hydraulic ram was placed on the top of the CFT beam-column specimen. The loading beam was placed on top of the ram, and was supported by two axial tension rods, which were anchored to the laboratory strong floor through a steel built-up section and pin-and-clevis type connection. The axial loading arrangement was free to rotate about the specimen base. The axial load (*P*) was applied along the chord of the laterally displaced shape of the CFT specimen, and maintained constant for the rest of the test. Additional descriptions and photographs of the test setup are provided in Hong (2007), and not included here for brevity.

Thermal loading (simulating the heating effects of standard E119 fire loading) was applied to the 0.3 m long base segment of the CFT specimen just above the concrete blocks. This base segment was the anticipated maximum moment and plastic hinge region. It was fire protected using gypsum plaster (6.4 mm thickness on metal lath) similar to the heat transfer specimens. The thermal loading was applied using the same heating and control equipment described in the heat transfer testing earlier.

Monotonically increasing lateral loading (*H*) was applied to the top of the specimen (at 0.15 m from the free end) after heating. The lateral loading was applied using a 900-kN capacity hydraulic ram that was attached to the laboratory reaction wall. Thus, the 1.65 m test length of the CFT specimen was subjected to constant axial loading, heating in the anticipated plastic hinge region, and monotonically increasing lateral loading.

Fig. 4(a) shows the free body diagram of the test length of the beam-column specimen. As shown, the plastic hinge region at the base of the specimen was subjected to bending moment (*M*) calculated as the product of the applied lateral load (*H*) and the test length (*L*) without any second-

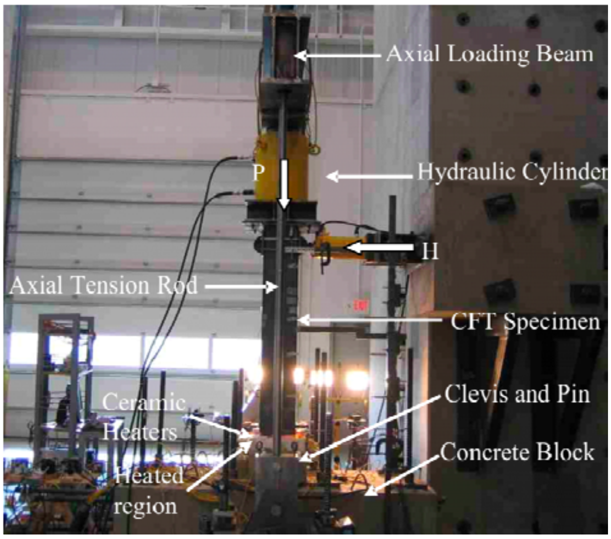

Fig. 3 Photograph of test setup for CFT beam-column experiments

order ($P\Delta$ or $P\delta$) moments. The axial force at the column base was equal to $P\cos\theta$, where θ was the chord rotation of the test length. The reduction in axial force was less than 1% for chord rotations (θ) up to 8-degrees and lateral displacement (Δ) at the top up to 0.14 L (235 mm). As shown later the maximum lateral displacements during the tests were less than 235 mm. The applied axial force (P) was maintained constant throughout the test using electronic control of the hydraulic valves and pump.

Table 2 shows the test matrix for the square CFT beam-column specimens subjected to combined structural and thermal loading. The parameters included in these tests were the section size (b = 254 or 305 mm), tube width-to-thickness ratio (b/t = 34 or 42), concrete strength (f'_c = 48 or 69 MPa), and heating duration (1h or 2h). The specimen nomenclature in Table 2 consists of the specimen width in inches, tube b/t ratio, axial load level (P/P_o) in percent, measured concrete strength (f'_c) in ksi, and the duration of heating. For example, CFT-10-34-15-7-1h is a CFT specimen with 10 in. (305 mm) square steel tube with b/t ratio equal to 34, axial load level equal to 15%, measured concrete strength equal to 7 ksi (48 MPa), and 1 hour of heating.

As shown in Table 2, three CFT beam-column specimens were tested at ambient temperatures. These tests provided control (base-line) data for evaluating the effects of elevated temperatures on behavior and for verifying analytical models at ambient temperatures. Ten CFT beam-column specimens were tested at elevated temperatures. After 1 hour of heating, the steel surface temperature was about 300°C. After 2 hours of heating, the steel surface temperature was close to 500°C. The specimen with no fire protection was heated for 30 minutes to achieve a surface temperature of about 535°C.

The CFT beam-columns specimens were made using commercially available steel tubes and ready mix concrete. All the specimens of the same type (width b and b/t ratio) were made from A500 Grade-B hollow structural shapes (HSS) manufactured from the same heat. Thus, there were four different A500 Grade-B steel heats corresponding to the four CFT specimen geometries that make up the complete test matrix of 13 specimens. Five uniaxial tension coupons were cut out

Table 2 Test-Matrix, Experimental Results, and Comparisons for CFT beam-column Specimens 1-13

No.	Specimen ID	Size ($mm \times mm$)	Measured (MPa)		b/t	P/P_o (%)	Axial load (kN)	Steel temp (°C)	Heating details	M_u (kN-m)	EI_{sec} (kN-m^2)	M_u/M_{EC4}	$EI_{sec}/EI_{cr\text{-}tr}$
			F_y	f'_c									
1	CFT-10-34-15-7	254 × 8	331	48	34	16	796	20	Ambient	312	17235	1.08	0.88
2	CFT-10-34-15-10	254 × 8	331	69	34	17	974	20	Ambient	339	18660	1.09	0.87
3	CFT-10-42-15-7	254 × 6.4	372	48	42	17	792	20	Ambient	295	16676	1.09	1.07
4	CFT-10-34-15-7-1h	254 × 8	331	48	34	16	814	300	1 hour	265	12155	0.92	0.62
5	CFT-10-34-15-7-2h	254 × 8	331	48	34	16	810	500	2 hour	190	9434	0.66	0.48
6	CFT-10-34-30-7-1h	254 × 8	331	48	34	36	1686	303	1 hour	237	12301	0.83	0.57
7	CFT-10-34-30-7-2h	254 × 8	331	48	34	34	1624	479	2 hour	165	8247	0.57	0.38
8	CFT-10-34-15-10-2h	254 × 8	331	69	34	17	983	475	2 hour	217	7719	0.70	0.36
9	CFT-10-34-30-10-2h	254 × 8	331	69	34	31	1730	486	2 hour	181	7753	0.56	0.33
10	CFT-10-42-15-7-2h	254 × 6.4	372	48	42	17	778	471	2 hour	190	6877	0.70	0.41
11	CFT-12-34-15-7-2h	305 × 9.5	351	48	34	16	1090	418	2 hour	390	22639	0.74	0.56
12	CFT-12-41-15-7-2h	305 × 8	358	48	41	16	1028	453	2 hour	325	15193	0.70	0.42
13	CFT-12-41-15-7-B	305 × 8	358	48	41	16	1041	535	No fireproofing	258	11223	0.56	0.31

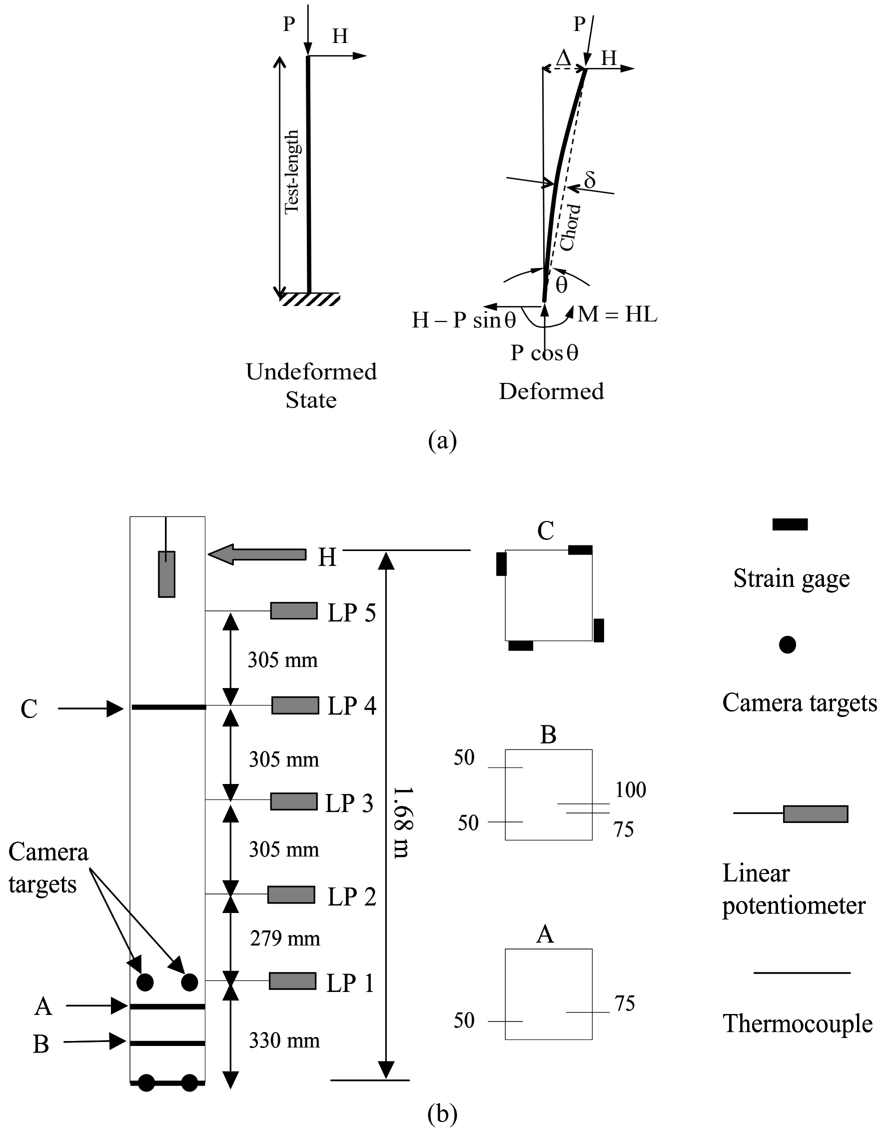

Fig. 4 Instrumentation layout for CFT beam-column specimens

from the sides of each steel tube type and tested according to ASTM E8 to determine mechanical properties and the stress-strain curves. The results from these uniaxial tension tests are presented in detail in Hong (2007). Table 2 includes the averaged yield stress for the four steel tube types.

Two different concrete strengths were used in the experimental investigations. All the CFT beam-columns specimens with the same concrete strength were filled with concrete from the same mix batch. Concrete cylinders were cast and tested to determine the 28-day compressive strengths and the compressive strength prior to the day of test. The averaged measured compressive strengths prior to the day of test are included in Table 2.

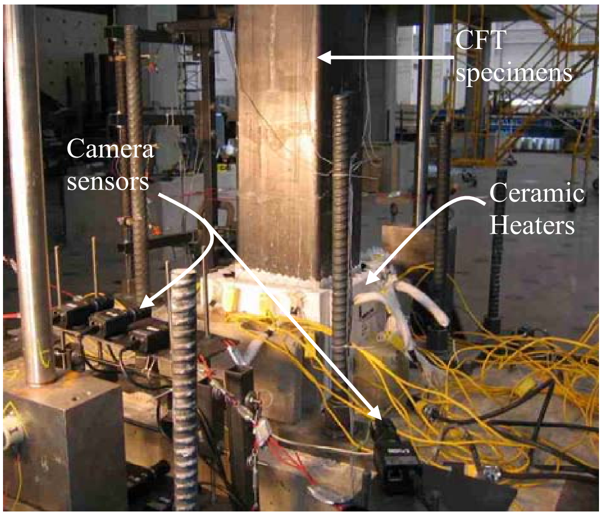

Fig. 5 Photograph of digital imaging and heating system

6.2 Instrumentation and deformation measurements

Fig. 4(b) shows the instrumentation layout for the CFT beam-column specimens. The lateral displacements and axial shortening of the specimen were measured using displacement transducers placed along the length and at the top. The rotations of the axial tension rods, which represented the chord rotation of the specimen, were measured using rotation meters placed on the clevis. Longitudinal strain gages were placed close to the top of the specimen. These were used to check the axial load alignment. Fig. 4(b) includes the thermocouple layout for the beam-column specimens. As shown, temperatures were measured on the gypsum plaster surface, steel tube surfaces, and the locations inside the concrete infill. Temperatures were measured at the middle and top planes of the heating region.

The deformations and curvature of the plastic hinge at the base were measured using the digital imaging system presented earlier. Fig. 5 shows a photograph of the digital imaging and heating system, and Fig. 6 shows the locations of the target points for the CFT beam-column tests. As shown in Fig. 6, six target points were defined on the surface of web plates above and below the heaters (i.e., outside of the heated zone). During the test, digital cameras were used to monitor the entire path of moving target points. The experiments were terminated when targets were not visible due to a large base rotation of the specimen. The heaters eventually covered the targets when the lateral displacement at the top of the specimen reached about 160 mm as shown in Fig. 7(c). The lateral displacements in Fig. 7(c) were measured using linear displacement transducers. Fig. 7(d) shows an example of the measured moment-curvature behavior of the CFT specimen, where the curvature of the plastic hinge was obtained using the digital imaging system and the moment was calculated using the applied lateral load (H) and distance to the center of the plastic hinge.

To calculate the curvature and the average strains, the displacements over the heated zone were measured under the following conditions. Digital cameras were perpendicular to the point and the plane of movement. The distance between the target point and the digital cameras was 450 mm.

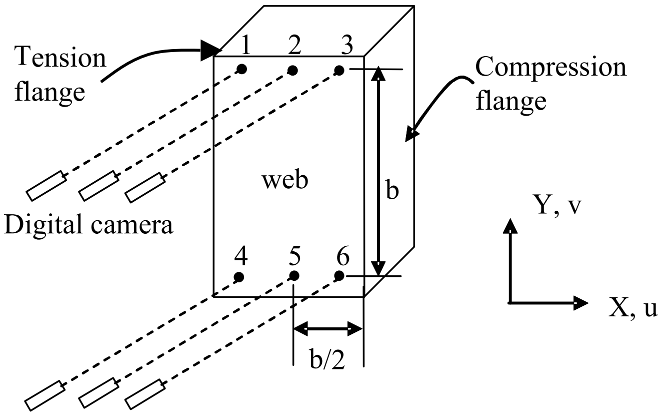

Fig. 6 Schematic of digital imaging camera layout

During the experiment, images were acquired every second, and the digital image correlation (DIC) program in the Labview-vision was used to determine the displacements (u_i and v_i) of each target point in the lateral and longitudinal directions. The longitudinal displacements (v_i) were used to estimate the average longitudinal strains ε_{avg-i} using Eqs. (1)-(3), and the average curvature (ϕ) of the plastic hinge region using Eq. (4).

$$\varepsilon_{avg-1} = \frac{v_3 - v_6}{d_{3,6}} \tag{1}$$

$$\varepsilon_{avg-2} = \frac{v_2 - v_5}{d_{2,5}} \tag{2}$$

$$\varepsilon_{avg-3} = \frac{v_1 - v_4}{d_{1,4}} \tag{3}$$

$$\phi = \frac{-\varepsilon_{avg-1} + \varepsilon_{avg-3}}{l_{1,3}} \tag{4}$$

In Eqs. (1)-(4), $d_{i,j}$ is distance between top and bottom rows of target points, and $l_{1,3}$ is the lateral distance between digital imaging points 1 and 3.

Conventional voltage-based sensors (e.g., rotation meters, strain gauges, and displacement transducers) were also used to measure the deformations of the unheated plastic hinge regions in the three ambient CFT beam-column specimens. The results from these measurements were compared to verify the deformations measurements using the digital imaging system. These comparisons are presented in detail in Hong (2007), and not repeated here for brevity.

7. CFT beam-column test results

The experimental results from the CFT beam-column tests include the thermal (*T-t*) responses of the steel tube and locations inside the concrete infill, the lateral load-displacement response of the CFT specimen, and the moment-curvature response of the plastic hinge region at the base of the specimens. For example, the experimental behavior and results for Specimen 7, i.e., CFT-10-34-15-7-2h is presented as follows. The behavior of the remaining specimens was very similar to that presented in the following sub-section.

7.1 Behavior and results for specimen CFT-10-34-30-7-2h

The geometric and material parameters for Specimen CFT-10-34-15-7-2h were provided in Table 2. The specimen was subjected to axial load equal to 1624 kN, which is approximately 34% of the section axial load capacity (P_o). The concentricity of the axial load was verified using four longitudinal strain gages that were distributed around the steel tube cross-section (i.e., one on each side). The specimen was subjected to thermal loading for 2 hours till the steel surface temperature underneath the gypsum plaster reached about 500°C. Steam and water emanated from the base of the specimen and from the vent holes in the specimen due to the evaporation of moisture from concrete. After heating, the specimen was subjected to the monotonically increasing lateral loading at the top.

Fig. 7(a) shows the measured gypsum and steel surface *T-t* curves. Fig. 7(b) shows some of the measured concrete infill temperatures. The specified and measured gypsum (exposed) surface *T-t* curves were almost identical. The gypsum surface temperatures on all sides of the base segment were about 980°C after two-hours of heating. The measured steel surface temperatures at the middle plane of the base segment were about 500°C. The measured concrete temperatures at the middle plane of the base section are about 290, 175, and 160°C at 50, 75, and 100 mm depth. The measured temperatures of the concrete infill at the top plane were similar but marginally higher than the measured temperature at the middle plane. This was probably because the thermocouples in the top plane had moved (bent down) slightly during concrete casting. Since the concrete temperatures have a significant gradient, small shifts can produce large variations in temperature.

Fig. 7(c) shows the measured lateral force-lateral displacement response of the specimen at the top. The lateral displacement plotted in the figure was measured 1.5 m above the fixed base. The specimen reached its lateral load capacity of approximately 102 kN at a lateral displacement of about 25 mm. The specimen maintained its lateral capacity with increasing displacements. Fig. 7(d) shows the measured moment-curvature (M-ϕ) response of the plastic failure segment of the specimen. The figure includes the graphical definition of moment capacity (M_u) for the specimen, which was equal to 165 kN-m. Table 2 includes the M_u value for the specimen, and its comparison with M_{EC4}, which is the ambient moment capacity of the specimen calculated using Eurocode 4 (ECS 2004) provisions. The comparison in Table 2 shows that at elevated temperatures, the moment capacity (M_u) decreased to about 57% of the ambient moment capacity (M_{EC4}).

The flexural stiffness (EI_{sec}) of the specimen was computed as the secant slope of the experimental M-ϕ curve corresponding to the moment value of $0.6M_u$. The moment value of $0.6M_u$ was used because the corresponding section flexural stiffness (EI_{sec}) will be used in the design or analysis process along with the estimated moment capacity at elevated temperatures. Table 2 includes the EI_{sec} value calculated for the specimen and its comparison with $EI_{cr\text{-}tr}$, which is the cracked transformed moment of inertia corresponding to $0.6M_{EC4}$, where M_{EC4} is the estimated

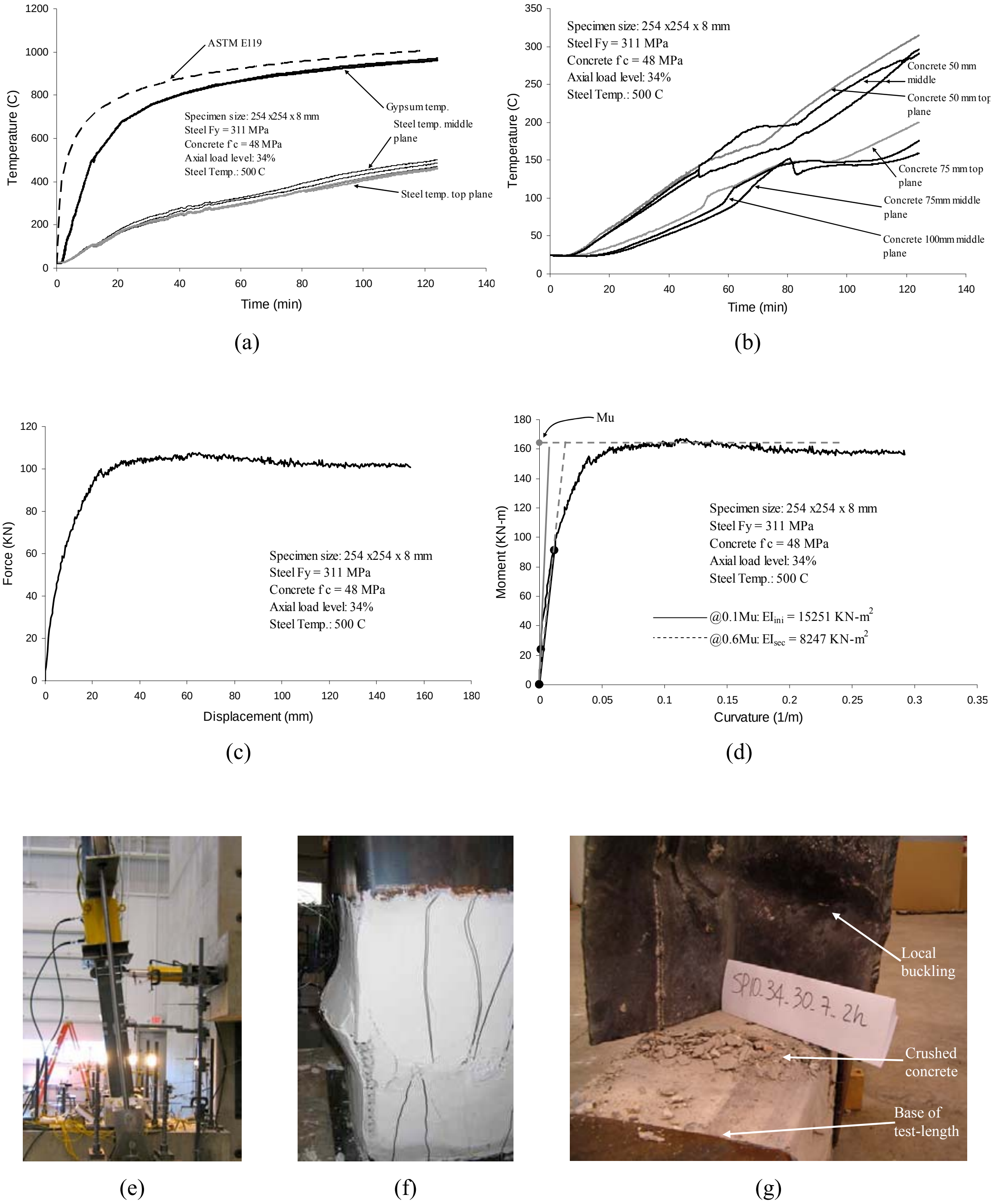

Fig. 7 Experimental results for specimen CFT10-34-30-7-2h: (a) gypsum and steel surface *T*-*t* curves; (b) concrete infill *T*-*t* curves; (c) lateral load – displacement responses; (d) moment-curvature response; (e) deformed shape at end of test; (f) local buckling in plastic hinge region; (g) concrete crushing in plastic hinge region

ambient moment capacity. The comparison in Table 2 indicates that that at elevated temperatures, the flexural stiffness (EI_{sec}) decreased to about 38% of $EI_{cr\text{-}tr}$.

Fig. 7(e) shows the overall deformed shape of the specimen at the end of the test. Fig. 7(f) shows the local buckling of the steel tube in the heated plastic hinge region. This local buckling was observed at the end of the test upon removal of the radiant heaters. The steel tube was removed to further inspect the concrete infill in the heated plastic hinge region of the specimen. Fig. 7(g) shows the extensive crushing of the concrete infill in the plastic hinge region of the specimen underneath the locally buckled steel tube. The local failures shown in Figs. 7(f)-(g) are very similar to those of ambient specimens with the exception that the concrete in the plastic hinge regions was very dry.

7.2 Summary of experimental results

The behavior of all the heated CFT beam-column specimens was similar to that described above for Specimen CFT-10-34-15-7-2h. All the specimens failed with the formation of local buckling and concrete crushing in the plastic hinge regions as shown in Figs. 7(e)-(g). The experimental results including: (1) the measured *T-t* responses for the gypsum plaster, steel tube surfaces, and points inside the concrete infill; (2) the measured lateral load-lateral displacement responses; (3) the lateral displacement profiles at different load values; and (4) the moment-curvature (M-ϕ) responses for the plastic hinge regions were obtained for all the tested specimens. These results and the experimental behavior for all beam-column specimens are presented in detail in Hong (2007) and not discussed here for brevity.

Figs. 8(a)-(c) show the moment-curvature (M-ϕ) responses of the plastic hinge regions of all the tested specimens. The values of curvature in Fig. 8 were calculated using the displacements measured using the digital imaging system and Eqs. (1)-(4). The specimen numbers identified in

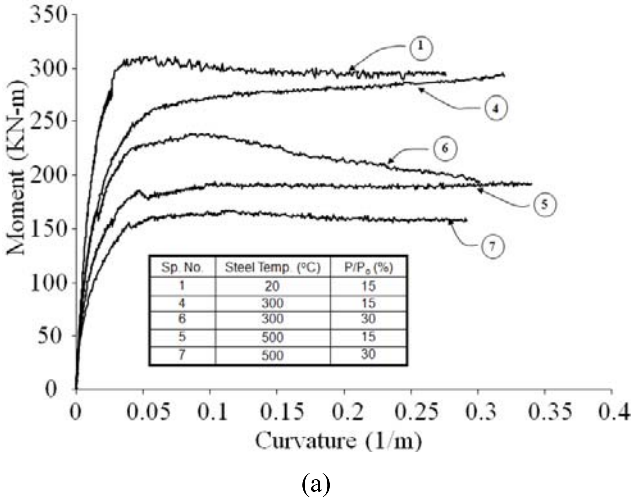

(a)

Fig. 8 Measured moment-curvature (M-ϕ) responses for specimens: (a) Specimens 1, 4, 5, 6, 7; (b) Specimens 2, 8, 9; and (c) Specimens 10, 11, 12, 13 listed in Table 1

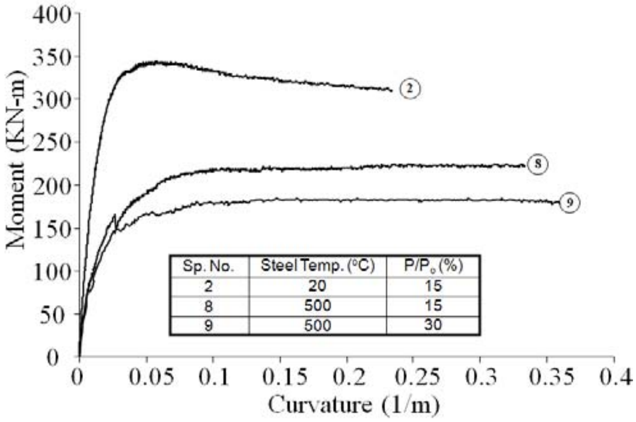

(b)

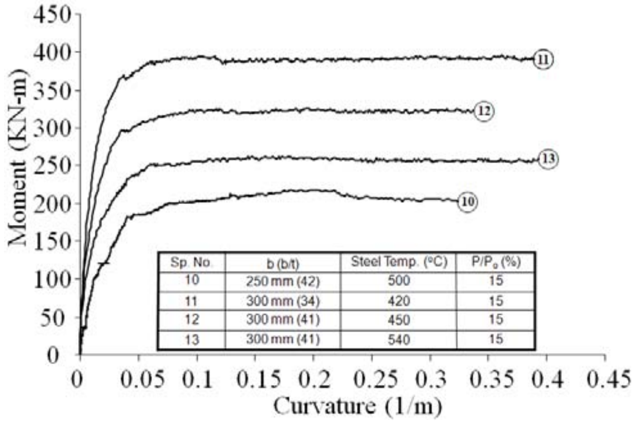

(c)

Fig. 8 Continued

Figs. 8(a)-(c) are in accordance with the specimen numbers in Table 2. Fig. 8(a) presents the M-ϕ responses for Specimens 1, 4, 5, 6, and 7. These specimens have the same steel tube width of 254 mm, width-to-thickness ratio of 34, and concrete infill strength of 48 MPa. They were subjected to different axial load levels and heating (steel surface temperatures). Fig. 8(b) presents the M-ϕ responses for Specimens 2, 8, and 9. These specimens have the same tube width of 254 mm, width-to-thickness ratio of 34, and concrete infill strength of 69 MPa. They were subjected to the same heating, but different axial load levels. Fig. 8(c) shows the M-ϕ responses for Specimens 10, 11, 12, and 13. These specimens have different sizes, b/t ratios, but the same concrete infill strength of 48 MPa and heating duration of 2 hours.

Table 2 includes the experimental results for all the CFT beam-column specimens including the moment capacities (M_u) and the secant flexural stiffness (EI_{sec}). The Table also includes the moment capacities (M_u) normalized with respect to the computed ambient moment capacities (M_{EC4}), and EI_{sec} normalized with respect to the cracked transformed moment of inertia ($EI_{cr\text{-}tr}$)

corresponding to $0.6M_{EC4}$. The results and comparisons in Table 2 show that the moment capacities (M_u) of ambient Specimens (1-3) are predicted conservatively using Eurocode 4 provisions. Elevated temperatures reduce the moment capacity (M_u) to 55-90% of the ambient moment capacity (M_{EC4}). Elevated temperatures also reduce the secant flexural stiffness (EI_{sec}) to 31-66% of the cracked transformed moment of inertia ($EI_{cr\text{-}tr}$).

7.3 Effects of parameters on strength and stiffness

The experimental results were used to evaluate the effects of various parameters, namely, the axial load level (P/P_o), concrete strength (f'_c), tube width (b), width-to-thickness (b/t) ratio, and steel surface temperature (T_s) on the moment capacity (M_u) and the secant flexural stiffness (EI_{sec}) of the CFT beam-column specimens. Fig. 9 shows variations of M_u/M_{EC4}, i.e., the normalized moment capacity, with respect to the axial load level (P/P_o), concrete strength (f'_c), tube b/t ratio, and steel surface temperature (T_s). Similarly, Fig. 10 shows variations of $EI_{sec}/EI_{cr\text{-tr}}$, i.e., the normalized flexural stiffness, with respect to the axial load level (P/P_o), concrete strength (f'_c),

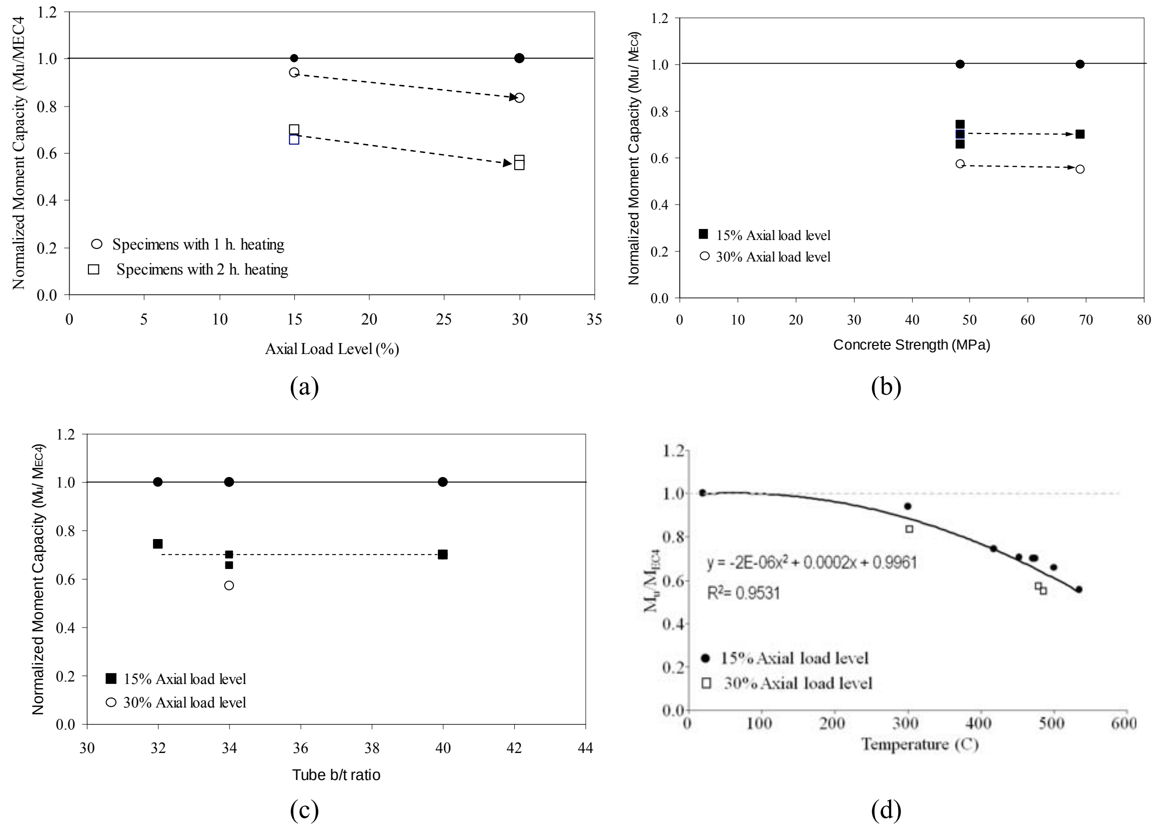

Fig. 9 Effects of various parameters on normalized moment capacity (M_u/M_{EC4}) of CFT beam-column specimens: (a) axial load level; (b) concrete strength; (c) tube b/t ratio; (d) steel surface temperature

tube b/t ratio, and steel surface temperature (T_s).

In Figs. 9-10, the normalized M_u/M_{EC4} and EI_{sec}/EI_{tr} for the ambient Specimens (1-3) are limited to 1.0 (instead of the computed values in Table 4) because the focus was on the effects of parameters on the behavior of heated specimens, and only a few limited ambient specimens were tested. Ambient specimens corresponding to each of the heated specimens (i.e., the same axial load level, b, b/t ratio, f_c') were not tested because the ambient behavior of CFT beam-columns is well known, and the Eurocode 4 provisions for computing their moment capacities are widely accepted (Varma *et al*. 2002).

Fig. 9(a) shows the normalized moment capacity (M_u/M_{EC4}) with respect to the axial load level (P/P_o in percent). As shown, the decrease in M_u/M_{EC4} depends mostly on the heating duration (or the steel surface temperature achieved T_s); and for the same heating duration, the decrease is slightly greater for the specimens with the higher axial load level (P/P_o). Fig. 9(b) shows that the decrease in M_u/M_{EC4} does not depend significantly on the concrete strength. Fig. 9(c) shows that the decrease in M_u/M_{EC4} does not depend significantly on the tube width-to-thickness (b/t) ratio. A similar plot of M_u/M_{EC4} with respect to the tube width (not shown here) shows that the decrease in M_u/M_{EC4} does not depend significantly on the tube width (b) or width-to-thickness (b/t) ratio.

Fig. 9(d) shows the strong correlation between the normalized moment capacity (M_u/M_{EC4}) and the steel surface temperature (T_s). It includes the data for CFT Specimen 13 with unprotected or exposed steel tube, which fits in quite well with the rest of the data. Eq. (5) was obtained by performing a regression analysis to establish the relationship between M_u/M_{EC4} and T_s. Eq. (5) had an R-squared value of 0.95, which implies that M_u/M_{EC4} is governed strongly by the steel surface temperature (T_s). The figure distinguishes between specimens with 15% and 30% axial load. It illustrates that the axial load level is the other parameter that has a slight influence on the normalized moment capacity. Fig. 9(d) further illustrates that the normalized moment capacity does not depend on the width (b) or b/t ratio.

$$M_u / M_{EC4} = -2E-06(T_s)^2 + 0.0002T_s + 0.9961 \tag{5}$$

Fig. 10(a) shows the normalized flexural stiffness ($EI_{sec}/ET_{cr\text{-}tr}$) with respect to the axial load level (P/P_o in percent). As shown, the decrease in the normalized flexural stiffness depends mostly on the heating duration (steel surface temperature achieved T_s) and not on the axial load level. Fig. 10(b) shows that the decrease in $EI_{sec}/EI_{cr\text{-}tr}$ depends slightly on the concrete strength. This decrease is slightly greater for the specimens with the higher concrete strength, especially at the lower axial load level of 15%. Fig. 10(c) shows that the decrease in $EI_{sec}/EI_{cr\text{-}tr}$ does not depend significantly on the tube width-to-thickness (b/t) ratio. A similar plot of $EI_{sec}/EI_{cr\text{-}tr}$ with respect to the tube width (not shown here) shows that the decrease in the normalized flexural stiffness does not depend significantly on the tube width (b).

Fig. 10(d) shows the strong linear correlation between the normalized flexural stiffness ($EI_{sec}/EI_{cr\text{-}tr}$) and the steel surface temperature (T_s). The figure includes the data for CFT specimen 13 with unprotected or exposed steel tube, which also fits in quite well with the rest of the data. Eq. (6) was obtained by performing a regression analysis to establish the relationship between $EI_{sec}/EI_{cr\text{-}tr}$ and T_s. Eq. (6) has a R-squared value of 0.98, which implies that $EI_{sec}/EI_{cr\text{-}tr}$ is governed mostly by the steel surface temperature (T_s), and does not depend significantly on other parameters.

$$EI_{\sec} / EI_{cr-tr} = -0.0013T_s + 1.0235 \tag{6}$$

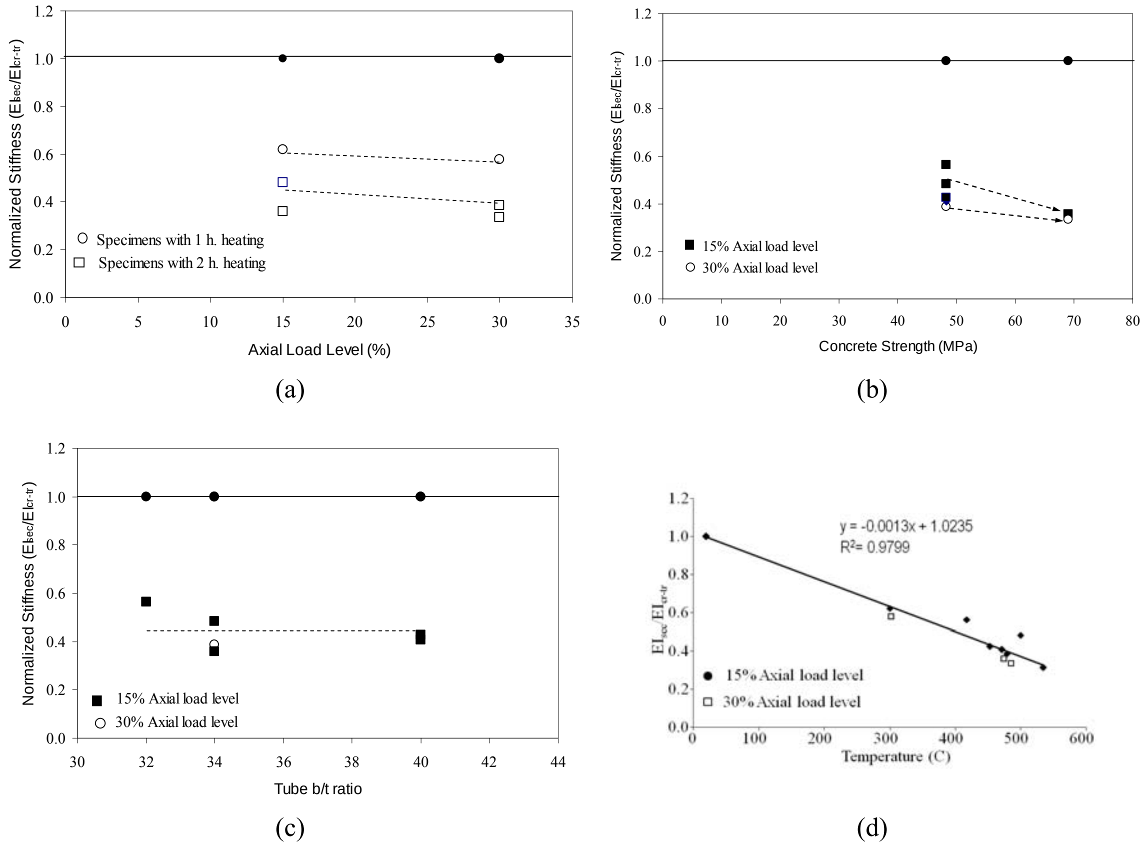

Fig. 10 Effects of various parameters on normalized flexural stiffness ($EI_{sec}/EI_{cr\text{-}tr}$) of CFT beam-column specimens: (a) axial load level; (b) concrete strength; (c) tube *b*/*t* ratio; (d) steel surface temperature

8. Conclusions

This paper presented a new experimental approach to determine the fundamental thermal and structural behavior of structural members subjected to elevated temperatures from fire loading. The experimental approach involved the use of innovative heating and control equipment that can be combined with hydraulic loading equipment in a laboratory environment to conduct combined heating and structural loading tests. The equipment uses radiation-based heaters that can be assembled around the test specimen, and controlled to subject the exposed structural surfaces to target *T*-*t* curves.

The experimental approach also involved the use of close range photogrammetry and digital image correlation to measure the deformations of heated portions of the structural member. Traditional voltage based sensors cannot be used easily to measure the deformations of structural members subjected to fire loading. Therefore, a non-contact digital image correlation technique was calibrated and used to measure the deformations of target points in the heated regions of the structural member.

The experimental approach was used to determine the fundamental moment-curvature (M-ϕ) behavior of CFT beam-column members subjected to elevated temperatures from fire loading, and to evaluate the effects of various parameters (axial load level, tube width, width-to-thickness ratio, and concrete strength) on their strength and stiffness at elevated temperatures. Thirteen CFT beam-column specimens were tested by subjecting them to constant axial loading (15-30% of capacity), heating for 1-2 hours simulating the E119 *T-t* curve in the anticipated plastic hinge region, and monotonically increasing lateral loading.

The experimental results for each CFT beam-column specimen included the *T-t* responses of the steel tubes and points inside the concrete infill, overall lateral load-displacement response, moment-curvature response of the plastic hinge region, moment capacity (M_u) and flexural stiffness (EI_{sec}) corresponding to $0.6M_u$. These experimental results provide knowledge of the fundamental behavior of CFT members subjected to elevated temperatures from fire loading, and can be used to verify new or existing analytical models for predicting the behavior of CFT members (beam-columns or columns) under fire loading (e.g., Agarwal and Varma (2011), Hong and Varma (2009, 2010)).

The experimental moment capacities (M_u) and flexural stiffness (EI_{sec}) were normalized with respect to the estimated ambient moment capacity (M_{EC4}) and flexural stiffness ($EI_{cr\text{-}tr}$) based on the cracked transformed moment of inertia corresponding to $0.6M_{EC4}$, respectively. These normalized moment capacities (M_u/M_{EC4}) and flexural stiffness ($EI_{sec}/EI_{cr\text{-}tr}$) were used to evaluate the effects of parameters included in the experimental investigations. These evaluations indicate that within the range of parameters included in the tests, the normalized moment capacity (M_u/M_{EC4}) and flexural stiffness ($EI_{sec}/EI_{cr\text{-}tr}$) depend primarily on the steel surface temperature (T_s). The other parameters (axial load level and concrete strength) have a small influence on M_u/M_{EC4} and $EI_{sec}/EI_{cr\text{-}tr}$, and the tube width and width-to-thickness ratio seem to have almost no influence.

Regression analysis of the test results was used to develop equations relating the normalized moment capacity (M_u/M_{EC4}) and flexural stiffness ($EI_{sec}/EI_{cr\text{-}tr}$) to the steel surface temperature (T_s). These equations can be used to estimate the flexural stiffness and moment capacity of CFT beam-columns subjected to elevated temperatures from fire loading. They can also be used to develop a simple bilinear (elastic-perfectly plastic) model of the moment-curvature behavior of CFT beam-column specimens at elevated temperatures.

The experimental approach presented in this paper can be used to conduct similar research and develop knowledge of the fundamental behavior of other structural members subjected to fire loading(e.g., Choe *et al*. (2011)).

Acknowledgments

The research presented in this paper was funded by the National Science Foundation (Grant No. CMS-0453913 and 0601201), and the U.S. Department of Commerce through the Extramural Fire Research Grant Program administered by the National Institute of Standards and Technology, Building and Fire Research Laboratory (NIST-BFRL). Experimental data, findings, and conclusions or recommendations are those of the authors only.

References

Agarwal, A. and Varma A.H. (2011), "Design of steel columns at elevated temperatures due to fire: Effects of rotational restraints", *Eng. J.*, *AISC*, 297-314.

AISC (2003), *Design Guide 19 – Fire Resistance of Structral Steel Framing*, (eds. Ruddy, J.L., Ioannides, S. A.), AISC, Chicago, IL, USA.

ASCE (2007), *Standard Calculation Methods for Structural Fire Protection*, ASCE/SEI/SFPE 29-05, ASCE, Reston, VA, USA.

ASTM (2010), *Standard Test Methods for Fire Tests of Building Construction and Materials*, Active Standard ASTM E119, American Society for Testing and Materials, W. Conshohocken, PA, USA.

Beyler, C.L., Beitel, J., Iwankiw, N. and Lattimer, B. (2007), "Fire resistance testing for performance-based fire design of buildings", *NIST GCR 07-971*, Gaithersburg, MD, USA, pp. 154.

Choe, L. (2011), "Structural mechanics and behavior of steel members under fire loading", Ph.D. Dissertation, School of Civil Engineering, Purdue University, West Lafayette, IN, USA.

Choe, L., Varma, A.H., Agarwal, A. and Surovek, A. (2011), "Fundamental behavior of steel beam-columns and columns under fire loading: An experimental evaluation", *J. Struct. Eng.*, *ASCE*, **137**(9), 954-966.

ECS (2004), Eurocode 4: Design of Steel and Concrete Structures, Part 1.1, General Rules and Rules for Buildings, European Committee for Standardization, Brussels, Belgium.

Han, L.H., Yang, Y.F. and Xu, L. (2002), "An experimental study calculation on the fire resistance of concrete filled SHS and RHS columns", *J. Constr. Steel Res.*, **59**(4), 427-452.

Hong, S. (2007), "Fundamental behavior of stability of CFT columns under fire loading", Ph.D. Dissertation, School of Civil Engineering, Purdue University, West Lafayette, IN, USA.

Hong, S. and Varma, A.H. (2009), "Analytical modeling of the standard fire behavior of loaded CFT columns", *J. Constr. Steel Res.*, **65**(1), 54-69.

Hong, S. and Varma, A.H. (2010), "Predicting fire behavior of composite CFT columns using fundamental section behavior", *J. ASTM Int.*, **7**(1), 23.

Huo, J., Zeng, X. and Xiao, Y. (2011), "Cyclic behaviors of concrete-filled steel tubular columns with pre-load after exposure to fire", *J. Constr. Steel Res.*, **67**(4), 727-739.

IBC (2009), *International Building Code*, International Code Council, Inc., Falls Church, VA, USA.

ISO-834 (1980), *Fire Resistance Tests – Elements of Buiding Construction*, International Standards Organization, Geneva, Switzerland.

Kodur, V., Garlock, M. and Iwankiw, N. (2008), "National workshop on structures in fire: State- of-the-art, research and training needs", *NIST GCR 07-915*, NIST, U.S. Department of Commerce, Gaithersburg, MD, USA, pp. 55.

Kodur, V.R. and MacKinnon, D.H. (2000), "Design of concrete-filled hollow structural steel columns for fire endurance", *Eng. J.*, **37**(1), 13-24.

Lu, H., Han, L.H. and Zhao, X.L. (2010a), "Fire performance of self-consolidating concrete filled double skin steel tubular columns: Experiments," *Fire Safety J.*, **45**(2), 106-115.

Lu, H., Zhao, X.L. and Han, L.H. (2010b), "Testing of self-consolidating concrete-filled double skin tubular stub columns exposed to fire", *J. Constr. Steel Res.*, **66**(8-9), 1069-1080.

Maluk, C., Bisby, L.A., Terrasi, G., Krajcovic, M. and Torero, J.L. (2012a), "Novel fire testing methodology: Why, how and what now?", *Proceeding of the 1st International Conference on Performance Based land Life Cycle Structural Engineering*, Mini Symposium on Performance-based Fire Safety Engineering of Structures, Hong Kong, December.

Maluk, C. and Bisby, L.A. (2012b), "120 years of structural fire testing: Moving away from the status quo," *Invited Plenary Presentation at the II Fire Engineering Conference*, Valencia, Spain, October.

NFPA (2009), *Building Construction and Safety Code* – NFPA 5000, NFPA.

NIST NCSTAR 1A (2008), "Final report on the collapse of the World Trade Center Building 7", *NIST NCSTAR 1A,* NIST, U.S. Department of Commerce, Gaithersburg, MD, USA.

Patel, V.I., Liang, Q.Q. and Hadi, M.N.S. (2012). "Inelastic stability analysis of high strength rectangular concrete-filled steel tubular slender beam-columns," *Int. Multiscale Mech.*, *Int. J.*, **5**(2), 91-104.

Romero, M.L., Moliner, V., Espinos, A., Ibanez, C. and Hospitaler, A. (2011), "Fire behavior of axially loaded slender high strength concrete-filled tubular columns", *J. Constr. Steel Res.*, **67**(12), 1953-1965.

Sadek, S., Iskander, M.G. and Liu, J. (2003), "Accuracy of digital image correlation for measuring deformations in transparent media", *J. Comput. Civil Eng.*, **17**(2), 88-96.

Sakumoto, Y., Okada, T., Yoshida, M. and Taska, S. (1994), "Fire resistance of concrete filled fire resistant steel tube columns", *J. Mater. Civil Eng., ASCE*, **6**(2), 169-184.

Selden, K. (2010), *Evaluation of a CMOS Digital Camera for Structural Engineering Measurements*, Bowen Laboratory Research Report 2010-3, School of Civil Engineering, Bowen Laboratory, Purdue University, West Lafayette, IN, USA.

Sunder, S.S., Gann, R.G., Grosshandler, W.L., Averill, J.D., Bukowski, R.W., Cauffman, S.A., Evans, D.D., Gayle, F.W., Gross, J.L., Lawson, J.R., Lew, H.S., McAllister, T.P., Nelson, H.E. and Sadek, F. (2005), "Final report of the national consortium safety team on the collapses of the World Trade Center Towers", *NIST NCSTAR 1*, NIST, U.S. Department of Commerce, Gaithersburg, MD, USA.

Varma, A.H., Ricles, J.M., Sause, R. and Lu, L.W. (2002), "Experimental behavior of high strength square Concrete Filled Steel Tube (CFT) columns", *J. Struct. Eng., ASCE*, **128**(3), 309-318.

Varma, A.H., Srisa-Ard, J. and Hong, S. (2004), "Behavior of CFT columns and beam-column under fire loading", *Proceedings of the Annual Stability Conference*, Structural Stability Research Council, University of Missouri, Rolla, 557-580.

Walz, J., Surovek, A., Agarwal, A., Choe, L. and Varma, A.H. (2011), "Closed-form characterization of fundamental section response of steel columns subjected to realistic fire loading", *Proceeding of Annual Stability Conference*, Structural Stability Research Council, Pittsburgh.

Xu, Y., Fu, Y., Zhang, Y. and Zhao, X. (2011), "Fire resistance of crisscross concrete filled steel tube core columns in the different axial compression", *Adv. Mater. Res.*, **163-167**, 157-160, Trans Tech Publication, Switzerland.

CC